Surfaces and Interfaces 26 (2021) 101353

Contents lists available at ScienceDirect

Surfaces and Interfaces

journal homepage: www.sciencedirect.com/journal/surfaces-and-interfaces

Tailoring CO_2 adsorption and activation properties of ceria nanocubes by coating with nanometre-thick yttria layers

Adrián Barroso Bogeat [a,b,c,*], Ginesa Blanco [a,b], José María Pintado [a,b], Daniel Goma [a,b], José Juan Calvino Gámez [a,b]

[a] Departamento de Ciencia de los Materiales e Ingeniería Metalúrgica y Química Inorgánica, Facultad de Ciencias, Universidad de Cádiz, Campus Río San Pedro s/n, 11510 Puerto Real (Cádiz), Spain

[b] Instituto Universitario de Investigación en Microscopía Electrónica y Materiales (IMEYMAT), Facultad de Ciencias, Universidad de Cádiz, Campus Río San Pedro s/n, 11510 Puerto Real (Cádiz), Spain

[c] Departamento de Química Inorgánica, Facultad de Farmacia, Universidad de Salamanca, Campus Miguel de Unamuno, Licenciado Méndez Nieto s/n, 37007 Salamanca, Spain

ARTICLE INFO

Keywords:
Ceria
Yttria
Surface basicity
Surface reducibility
CO_2 adsorption
CO_2 activation

ABSTRACT

Ceria (CeO_2) is a ubiquitous component in catalysts for environmental protection processes, especially those devoted to CO_2 valorisation. Aimed at preparing ceria-based nanomaterials with enhanced CO_2 adsorption and activation properties, both the surface acid-base and redox features of ceria nanocubes were modulated by a novel, simple, wet chemistry synthetic strategy consisting of their coating with yttria (Y_2O_3) layers of variable thickness in the nanometre scale. The as-synthesised samples were characterised with special attention to their surface basicity and reducibility. Characterisation results revealed that the surface doping with yttria not only improved both the reducibility at low temperature and CO_2 adsorption capacity of ceria nanocubes, but also introduced a variety of basic sites with different strength. Finally, the careful control of the yttria layer thickness allowed to modulate these effects and thereby the ability of nanostructured ceria to adsorb and activate the CO_2 molecule.

1. Introduction

Since the middle of the 1970's, cerium dioxide (CeO_2), commonly known as ceria, has been extensively employed in the field of heterogeneous catalysis, either as catalyst on its own or much more frequently as support of a variety of metal-containing catalytic active phases and as structural or electronic promoter [1–5]. This extensive use is largely attributable to its excellent redox and acid-base properties, as well as its interactions with the supported metal phase.

Regarding redox properties, it is well-established the ability of ceria to reversibly exchange lattice oxygen with reactants under both oxidizing and reducing conditions, which is usually referred to as oxygen storage capacity (OSC) [5–8]. Such a behaviour is coupled to the reversible Ce^{4+}/Ce^{3+} redox pair, i.e., to the reducibility of ceria, which is strongly influenced by its textural [9–11] and structural [12,13] features. Based on this unique redox performance, ceria has become a ubiquitous component in catalyst formulations for a variety of chemical processes involving oxidation and/or reduction reactions and showing environmental and industrial interest. Among them, three-way catalysis (TWC), soot oxidation in diesel engine exhausts, and fluid catalytic cracking (FCC) should be highlighted as those traditionally most diffused and important in terms of establishment, economic relevance, and tonnage [2,5]. In addition to these, other catalytic oxidation processes, such as hydrocarbons and oxygenates reforming, water gas shift reaction (WGS), preferential oxidation of CO in the presence of excess hydrogen (PROX), and oxidation of HCl and volatile organic compounds (VOCs) are emerging applications in which ceria-based catalysts are currently receiving a great deal of attention and research effort [5,14,15]. As far as the acid-base features are concerned, ceria is well-known to be a moderately basic oxide [16–18], whose surface exhibits O^{2-} sites of variable basicity depending on their coordination [19] and thereby on the exposed facets and the particle shape [20]. Such basic sites can behave as catalytic active sites for a broad range of organic reactions [21]. In this connection, basic surface sites on pure ceria have been

* Corresponding author at: Universidad de Salamanca, Departamento de Química Inorgánica, Facultad de Farmacia, Campus Miguel de Unamuno, Licenciado Méndez Nieto s/n, 37007 Salamanca, Spain.

E-mail addresses: adrian.barroso@uca.es, adrianbogeat@usal.es (A. Barroso Bogeat).

https://doi.org/10.1016/j.surfin.2021.101353
Received 4 March 2021; Received in revised form 4 May 2021; Accepted 15 July 2021
Available online 24 July 2021

reported to promote the activation of hydrocarbons, like methane [1,22–24]. Finally, strong metal-support interaction (SMSI) effects have been also proved to play a pivotal role in the performance of ceria-supported metal catalysts [1,25–27]. In fact, the occurrence of this SMSI allows to improve the dispersion of the active metal phases, to modify both their electronic and chemical properties, and also to inhibit undesirable sintering phenomena, thus resulting in beneficial effects on the activity, selectivity, and durability of ceria-supported catalysts in a number of processes. Special mention should be made of those devoted to CO_2 valorisation, such as hydrogenation and reforming reactions, in which the specific metal-ceria interfaces may be very reactive and even behave as active sites [27,28].

On the other hand, it is worth highlighting that the above unique properties of ceria can be further modified in a controlled manner by several strategies, such as doping with other metal elements and morphological control. Concerning the first strategy, a large variety of dopants have been reported to replace a portion of the Ce^{4+} cations without altering the cubic fluorite-type structure typical of ceria, thereby resulting in the formation of solid solutions [5,6]. This doping has severe impact not only on the lattice parameters, but also on the oxygen vacancy formation energy as well as on both the surface basicity and redox properties [15]. Among the ceria dopants, rare earth elements (REEs, henceforward), a family of seventeen chemical elements encompassing the fifteen lanthanoids along with scandium and yttrium, have been widely investigated because as a rule they form solid solutions with ceria over a broad range of compositions [6,29,30]. More specifically, over the past few decades special attention has been paid to solid solutions of ceria and trivalent REE cations. These aliovalent dopants decrease the concentration of Ce^{3+} cations and increase both the number of oxygen vacancies and their mobility in the fluorite lattice, thus leading to high ionic conductivity values in the intermediate temperature range (i.e., from 400 to 700°C) for the resulting materials. On the basis of this remarkable and exploitable property, trivalent REE-doped ceria solid solutions have been profusely explored as suitable candidates for their application as electrolytes and electrodes in solid oxide fuel cells (SOFCs) and electrolysis cells (SOECs) [5,30,31]. As regards the second strategy, controlling the morphology and exposed facets is a well-established approach with a view to tuning the redox properties and catalytic performance of ceria. By using facile hydrothermal and solvothermal methods, it is possible to prepare crystalline ceria nanoparticles featuring various well-defined shapes, and even to adjust the ratio for certain facets [32,33]. Amongst the reported ceria nanoshapes, those enclosed by low-index surfaces have been by far the most widely investigated, i.e., nanocubes ({100}-facet dominant), nanorods ({110}-facet dominant), and nanooctahedra ({111}-facet dominant). According to the results of theoretical calculations, it is generally agreed that the above three facets, which are the most stable for ceria, differ in their relative thermodynamic stability by the order: {111} > {110} > {100}, so that their reactivity should follow just the opposite trend [20,34,35]. Moreover, the different coordination of O^{2-} and Ce^{4+} ions in these surfaces also affects their acid-base properties. Therefore, the three major facets of ceria are expected to display slightly different activity and/or selectivity in certain catalytic processes driven by the redox behaviour and/or the acid-base chemistry [20]. In fact, this facet-dependent catalytic activity of nanoshaped ceria particles has been evidenced in a great variety of reactions, like CO, soot, and VOC oxidation, methane dry reforming, methanol and ethanol reforming, low-temperature WGS, hydrogenation, and so on ([20] and references therein).

In recent years, reducing the global emissions of greenhouse gases, particularly CO_2, has become mandatory in order to tackle the climate change arising from global warming and to decrease the carbon footprint of today's society, while satisfying its ever-increasing demand of energy, fuels, and chemicals. Among the different strategies proposed to overcome this challenge, CO_2 conversion into a variety of high added value fuels and chemicals is broadly considered as the most attractive and promising alternative from both the environmental and economic standpoints [36]. In view of the high chemical stability of the CO_2 molecule, its conversion inevitably requires the application of catalytic processes, a large number of which are based on heterogeneous catalysis. In this regard, a number of works have revealed the ability of ceria to activate the CO_2 molecule under mild conditions by an oxygen vacancy-assisted mechanism, thus paving the way toward the design of novel heterogeneous catalysts for the valorisation of this greenhouse gas through different conversion reactions, such as hydrogenation, hydrocarbons reforming, and non-reductive transformations [27,35,37]. Under this context, the present work is aimed at pushing forward the rational design of novel high performance ceria-based catalysts for CO_2 conversion. On the basis of the aforementioned strategies commonly applied to further improve the catalytic properties of this lanthanoid oxide, we have envisaged a new synthetic approach to prepare ceria-based nanostructured materials featuring excellent adsorption capacity and interaction with the CO_2 molecule. Our strategy relies on depositing a nanometre-thick yttria (Y_2O_3) layer on the crystallographically well-defined surface of ceria nanocubes, and benefiting from the changes in both the redox and acid-base features of these latter imprinted by the supported phase. In addition to the relatively high solubility of the Y^{3+} cation into the ceria lattice, this REE has been selected as dopant because its incorporation increases the number of oxygen vacancies, thus enhancing the reducibility, while slightly decreasing the surface basicity due to the weak basic character of yttria. Finally, we have also demonstrated that the control of the yttria layer thickness is a very simple method which enables to modulate both the surface acid-base and redox properties of ceria and thereby its ability to adsorb and activate the CO_2 molecule.

2. Materials and methods

2.1. Synthesis of yttria-coated ceria nanocubes

The preparation of the Y_2O_3-coated CeO_2 NCs samples was accomplished in two successive stages by using facile surfactant-free wet chemistry procedures. First, CeO_2 NCs having an average edge length of around 30 nm were synthesized by a simple hydrothermal method, previously reported in the literature [38] and successfully applied by our research group for the preparation of both pure [39,40] and Ln-doped CeO_2 NCs, where Ln stands for La [41,42] and Pr [43]. Briefly, 125 mL of 17.3 mol·L^{-1} NaOH (99%, Scharlau) aqueous solution, 100 mL of 0.12 mol·L^{-1} $Ce(NO_3)_3{\cdot}6H_2O$ (99.5%, Alfa Aesar) aqueous solution, and 15 mL of deionised water were mixed in a polypropylene beaker and vigorously stirred for 30 min at room temperature by means of a magnetic stirrer. Next, the resulting greyish homogeneous suspension was carefully transferred into a 250 mL Teflon vessel, which was placed in a stainless steel autoclave reactor and tightly sealed. This reactor was heated at 180°C for 24 h in an electric oven. Once this time had elapsed, the system was allowed to slowly cool down to room temperature, and then the obtained yellowish solid, in a series of successive steps, was separated by centrifugation, thoroughly washed several times with deionised water until neutral pH of the liquid phase and once with absolute ethanol (VWR Chemicals, France), and oven-dried at 80°C for 24 h. The synthesis yielded around 1.9 g of CeO_2 NCs, so it was carried out in duplicate in order to obtain the required mass of product for later tasks, including its physico-chemical characterisation and coating with thin Y_2O_3 layers of varying thickness.

In a second stage, the as-synthesised CeO_2 NCs were coated with nanometre-thick Y_2O_3 layers, equivalent to Y/Ce atomic ratios of 0.1 and 0.2 in the resulting nanostructured materials (i.e., 10 and 20 at.%, respectively). For such an aim, a controlled chemical precipitation method, previously described in detail elsewhere [44] and also applied by our research group for the synthesis of both SiO_2-CeO_2 and ZrO_2--CeO_2 core@shell systems [45,46], was employed. $Y(NO_3)_3$ and hexamethylenetetramine (HMT, henceforth), which are both readily soluble

in water and ethanol, were used as Y_2O_3 precursor and precipitant agent, respectively. Thus, 1 g of the freshly prepared CeO_2 NCs and the appropriate amount of $Y(NO_3)_3{\cdot}4H_2O$ (99.99%, Sigma Aldrich, Germany) for attaining the targeted Y loadings in the final products were dispersed in 60 mL of ethanol (96%, VWR Chemicals, France) under ultrasonication for 30 min. The suspension was heated from room temperature up to 75°C under mechanical stirring of 800 rpm. Once this temperature had been reached, 20 mL of an aqueous solution containing the HMT mass corresponding to a HMT/Y^{3+} molar ratio of 5 was slowly added to the above suspension at a rate of 0.33 mL·min^{-1} by means of a highly precise syringe pump. After that, the reaction mixture was further aged for 1 h under the same heating and stirring conditions. The obtained solid was separated by centrifugation, repeatedly washed with deionised water and ethanol to remove any remnants of reagents, and oven-dried at 80°C overnight. Finally, the oven-dried product was ground in an agate mortar, sieved, and calcined in a muffle furnace at 370°C for 4 h with a heating rate of 5°C·min^{-1} to obtain the Y_2O_3-coated CeO_2 NCs.

The resulting samples will be hereinafter referred to as "XXY-CeO_2 NCs", where XX stands for the nominal atomic percentage of Y relative to Ce, i.e., 10 and 20 at.%.

2.2. Physico-chemical characterisation

The actual Y/Ce atomic ratio of the freshly prepared samples was estimated by X-ray fluorescence (XRF) analyses carried out in a M4 Tornado energy dispersive spectrometer from Bruker, equipped with Mo Kα radiation ($\lambda = 0.7107$ Å) source operating at 50 kV and 600 μA.

X-ray diffraction (XRD) patterns for both the pristine CeO_2 NCs and the Y_2O_3-coated samples were collected at room temperature in a D8 ADVANCE diffractometer from Bruker, operating with Cu Kα radiation ($\lambda = 1.5406$ Å) and under the following specific acquisition conditions: 2θ range from 10 to 90°, step size of 0.02°, and step counting time of 38.4 s. The software DiffracPlus was employed to determine the full width at half maximum (FWHM) of the (111) diffraction peak for cubic fluorite-type CeO_2, in order to estimate the mean (volume average) crystallite size (D) of this phase by applying the Scherrer equation, with a correction for instrument line broadening using quartz as pattern.

The specific surface area (S_{BET}) of the nanomaterials was assessed by applying the Brunauer, Emmet, and Teller equation [47] to their respective N_2 adsorption-desorption isotherms in the relative pressure ($p/p°$) range from 0.05 to 0.20. These isotherms were registered at -196°C using an ASAP 2020 equipment (Micromeritics). Prior to starting the adsorption-desorption measurements, about 100 mg of each powder sample was out-gassed under vacuum at 200°C for 4 h in order to remove moisture and any possible gases and vapours from the laboratory atmosphere adsorbed on the materials surface.

The freshly prepared nanomaterials were also characterised at micro- and nanoscale by a set of electron microscopy techniques, including high resolution transmission electron microscopy (HRTEM), high angle annular dark field-scanning transmission electron microscopy imaging (HAADF-STEM), and energy-dispersive X-ray spectroscopy (X-EDS). These analyses were carried out in a Talos F200X scanning transmission electron microscope (FEI, Thermo Scientific), equipped with a high efficiency X-EDS ChemiSTEM system implementing four windowless SDD detectors [48,49]. Previously, small amounts of the powdered samples, freshly prepared without any additional treatment, were deposited onto holey carbon-coated TEM grids. Processing and quantification of X-EDS data were performed by employing the Thermo Scientific Velox software (version 2.13).

Characterisation of the redox behaviour of both the CeO_2 NCs and the Y_2O_3-coated materials was accomplished by temperature-programmed reduction (TPR) followed by mass spectrometry (MS). TPR-MS studies were performed in a conventional experimental device coupled to a quadrupole mass spectrometer (Thermostar GSD301T1, Pfeiffer Vacuum) to accurately monitor the composition of the outlet gas stream. The amount of sample typically used in each of these essays was around 100 mg. Prior to the reduction experiments, all three samples were subjected to the following standard cleaning pretreatment: oxidation in a 60 cm^3·min^{-1} STP flow of O_2(5%)/He at 350°C for 1 h, followed by slow cooling down under the same oxidising atmosphere to approximately 150°C, and then the flow was switched to pure He for further cooling down to room temperature, thus avoiding oxygen adsorption on samples surface. After this pretreatment, the TPR-MS analyses were carried out in a flow of 60 cm^3·min^{-1} STP of H_2(5%)/Ar from room temperature up to 900°C at a heating rate of 10°C·min^{-1}. The samples were additionally kept at this maximum temperature for 1 h. The main mass/charge (m/z, henceforward) ratios recorded during these experiments were 2 (H_2^+) to monitor hydrogen consumption and 18 (H_2O^+) for the concomitant water evolution. In this connection, it should be pointed out that for the sake of simplicity TPR results are herein depicted as water evolution profiles, a complete consistency with the corresponding hydrogen consumption curves being found for all tested nanomaterials. The m/z ratios 28 (CO^+), 40 (Ar^+), and 44 (CO_2^+) were simultaneously followed.

Surface basicity (i.e., both the nature and concentration of basic sites) of the raw CeO_2 NCs and the corresponding Y_2O_3-coated samples was studied by temperature-programmed desorption (TPD) of pre-adsorbed CO_2 followed by mass spectrometry (MS). These TPD-MS diagrams were recorded in the same equipment previously employed for the TPR-MS essays. About 100 mg of powder sample was subjected to the aforementioned standard cleaning pretreatment in O_2(5%)/He at 350°C for 1 h. After cooling down to room temperature, the pretreated nanomaterial was exposed to a 60 cm^3·min^{-1} STP flow of pure CO_2 ($P_{CO2} = 1$ atm) for 1 h in order to saturate the sample surface with adsorbed CO_2. Then, the sample was flushed with a flow of 60 cm^3·min^{-1} STP of pure Ar at room temperature for 1 h to remove the physically adsorbed CO_2. Finally, the TPD-MS experiment was carried out in the same inert flow from room temperature up to 900°C at a heating rate of 10°C·min^{-1}. During this analysis, MS signals for m/z 12 (C^+), 28 (CO^+), 40 (Ar^+), and 44 (CO_2^+) were registered.

Furthermore, additional information regarding the surface basicity of the prepared nanomaterials was derived from CO_2 volumetric chemisorption experiments. The CO_2 isotherms were recorded on a Micromeritics ASAP 2020 apparatus and employing around 100 mg of sample. Once again, prior to the adsorption measurements the materials were pretreated in a O_2(5%)/He atmosphere at 350°C for 1 h, followed by 1 h-evacuation at the same temperature and under a residual pressure below 10^{-6} Torr. Then, two consecutive CO_2 isotherms were acquired at 35°C and over the partial pressure range from 0 to 760 Torr, with an evacuation treatment at identical temperature for 1 h in between them.

Table 1
Macroscopic chemical composition, average crystallite size, and specific surface area for the CeO_2 NCs and Y_2O_3-coated CeO_2 NCs.

Sample	Y_2O_3 / wt. %	CeO_2 / wt. %	Y/Ce / at. %	D / nm	S_{BET} / m^2·g^{-1}
CeO_2 NCs	-	100	-	34.5	21.0
10Y-CeO_2 NCs	5.8	94.2	9.3	27.5	18.0
20Y-CeO_2 NCs	11.5	88.5	19.8	28.9	18.8

3. Results and discussion

3.1. Macroscopic compositional, structural, and textural characterisation

Both freshly prepared Y_2O_3-coated CeO_2 NCs samples were analysed by the XRF technique in order to estimate their actual Y contents. Obtained quantification results are gathered in Table 1. As can be seen, dopant to cerium atomic ratios of 9.3 and 19.8% were found for 10Y-CeO_2 NCs and 20Y-CeO_2 NCs, respectively. These values are slightly

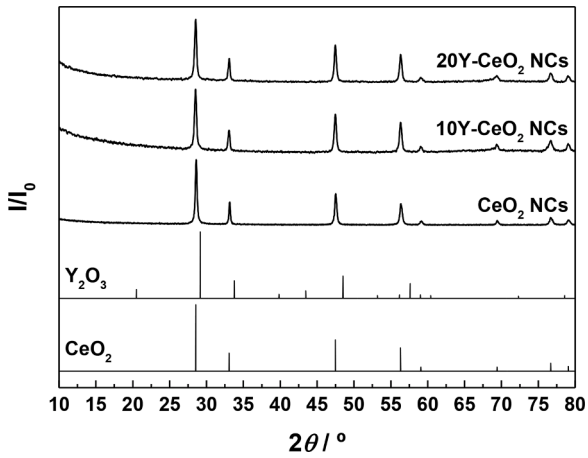

Fig. 1. XRD diagrams recorded for the freshly prepared CeO_2 NCs and XXY-CeO_2 NCs samples. Reference patterns for cubic fluorite CeO_2 and cubic Y_2O_3 have also been included in this figure for the sake of comparison.

lower but very close to the expected yttrium nominal loadings of 10 and 20 at.%, so for the sake of simplicity the Y-containing samples will be herein referred to as 10Y-CeO_2 NCs and 20Y-CeO_2 NCs. Accordingly, it becomes apparent that, at least in terms of the average macroscopic chemical composition of the resulting nanomaterials, the applied surfactant-free wet chemistry procedure was successful and achieved the ultimate synthetic goal.

The structure of the three prepared samples was first studied at a macroscopic scale by means of the powder XRD technique. The recorded diagrams are displayed in Fig. 1, in which the reference patterns corresponding to pure cubic fluorite CeO_2 (space group *Fm*-3*m*, JCPDS card number 34-0394) and cubic Y_2O_3 (space group *Ia*-3, JCPDS card number 89-5591) have been also included for comparison purposes. As can be seen from this figure, all three experimental diffractograms are dominated by a well-defined set of very intense and sharp reflections typical of CeO_2 with cubic fluorite-type structure. No diffraction peaks ascribable to crystalline phases other than this latter, and particularly to cubic Y_2O_3, are clearly identified in the corresponding diagrams after coating the raw CeO_2 NCs with thin Y_2O_3 layers. Such observation may be accounted for the extremely high dispersed state of the incorporated Y-containing phase on the surface of the CeO_2 NCs support and thereby its very small mean crystal domain size, likely below the detection limit of the powder XRD technique (i.e., around 4-5 nm) [50]. Furthermore, no evident shifts in the position of the main fluorite CeO_2 reflections are noticed for both yttria-coated samples, thus allowing to discard an effective incorporation of the REE dopant into the CeO_2 lattice during the calcination treatment in air at 370°C to yield solid solutions. This conclusion is additionally corroborated from an estimation of the lattice parameter carried out for both the bare CeO_2 NCs and the Y-containing materials by using the most intense diffraction peak, centred at around 28.5° and corresponding to the (111) crystallographic planes. As expected, obtained values for the lattice parameter are quite similar for all fresh nanomaterials, and very close to that reported for pure crystalline ceria (i.e., 5.41 Å). Finally, the application of the Scherrer equation leads to average crystallite sizes of around 30 nm (see fifth column in Table 1). In brief, all these observations are fully consistent with the presence in the coated samples of Y_2O_3-based surface phases, consisting of crystallites with nanometric dimensions in a highly dispersed state and evenly covering the CeO_2 nanocubes.

The N_2 adsorption-desorption isotherms measured for the pristine CeO_2 NCs and the freshly prepared yttria-coated materials have been plotted together in Fig. 2 for the sake of comparison. In accordance to the recently updated IUPAC classification [51], these isotherms by their shape can be considered as type IVa, which is typical of essentially mesoporous solids with negligible microporosity. In this regard, the absence of micropores in the nanostructured oxide samples is clearly evidenced by the very low N_2 adsorption at relative pressure (p/p^0) values below 0.1. Furthermore, all three isotherms display well-defined hysteresis loops in their desorption branches, a feature related with capillary condensation phenomena occurring in mesopores with sizes above 4 nm [51]. At this point, it should be noted that this mesoporosity observed in the samples is very likely to come from voids and gaps existing between closely spaced cubic nanoparticles, which gather forming aggregates. From Fig. 2 it also becomes evident that the measured physisorption isotherms are very similarly shaped, the only prominent modification affected the amount of adsorbed N_2 due to the different surface area of the nanomaterials. As expected, the deposition of the nanometre-thick yttria layers on the facets of the ceria nanocubes brings about a significant decrease in the specific surface area from 21

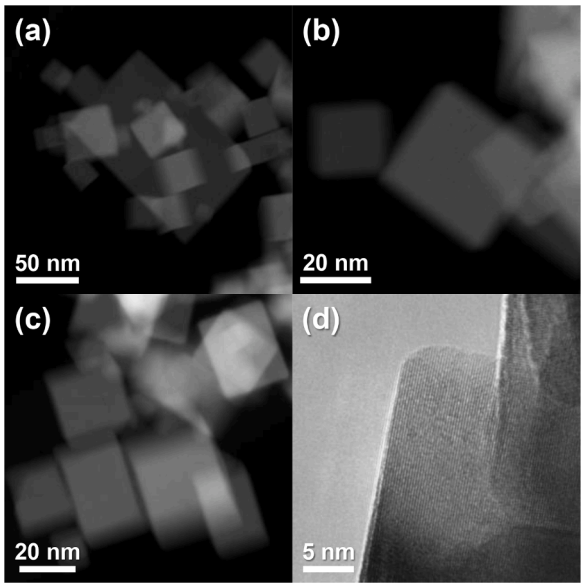

Fig. 3. Representative HAADF-STEM images for the as-prepared 10Y-CeO_2 NCs (a and b) and 20Y-CeO_2 NCs (c) samples. HRTEM image for the fresh 10Y-CeO_2 NCs sample (d).

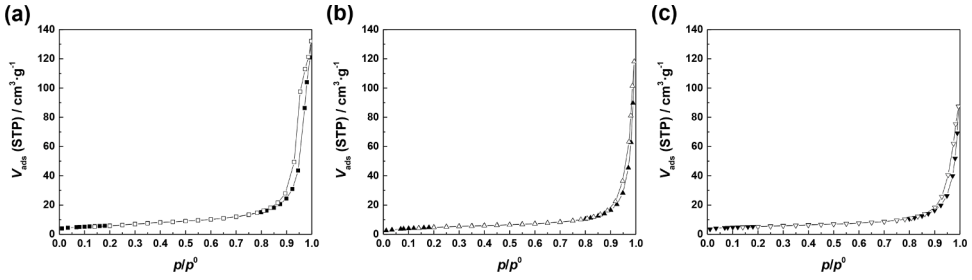

Fig. 2. N_2 adsorption-desorption isotherms registered at -196°C for the fresh nanostructured oxide samples: (a) CeO_2 NCs, (b) 10Y-CeO_2 NCs, and (c) 20Y-CeO_2 NCs.

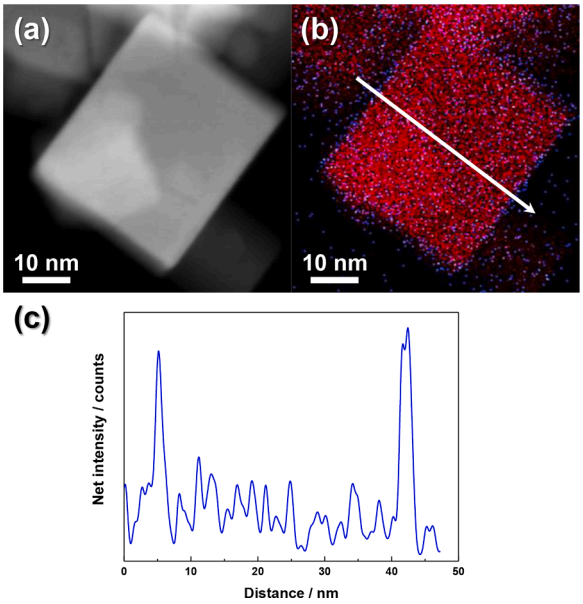

Fig. 4. (a) HAADF-STEM image for a single nanocube representative of the freshly prepared 20Y-CeO_2 NCs sample and (b) its corresponding X-EDS map showing the distribution of cerium (red) and yttrium (blue). (c) Line profile of yttrium acquired along the nanocube as indicated by the white arrow marked on (b).

$m^2 \cdot g^{-1}$ for these latter to around 18 $m^2 \cdot g^{-1}$ for both coated samples.

3.2. Morphological, nanocompositional, and nanostructural characterisation

Fig. 3 gathers representative HAADF-STEM and HRTEM images recorded for both as-prepared Y-containing nanostructured materials. First, it is observed that these samples in fact consist of cubic-shaped nanocrystals, the presence of any isolated nanoparticles or aggregates exclusively made up of Y_2O_3 being not detected. Furthermore, as can be seen from the corresponding HRTEM images the exposed surfaces of this couple of nanomaterials are predominantly dominated by (100) planes. Nevertheless, clearly visible truncations located at corners and edges and associated with (111) and (110) facets, respectively, are also detected in these micrographs. Such crystallographic description is essentially the same provided for the pristine CeO_2 NCs sample from an in-depth electron microscopy characterisation study (images not shown here for the sake of brevity), which is in turn well in agreement with that previously reported elsewhere for ceria nanocubes prepared by using an identical hydrothermal procedure [39]. Therefore, it may be concluded that neither the morphology nor the nanostructure of the starting CeO_2 NCs support apparently undergo noticeable changes as a result of the incorporation of the ultrathin Y_2O_3 layers by means of the surfactant-free controlled chemical precipitation method. Finally, HRTEM images acquired for both yttria-coated nanomaterials do not reveal the occurrence of tiny, randomly oriented, Y_2O_3 crystallites forming a nanometre-thick polycrystalline phase on the CeO_2 NCs surface, thus suggesting the adequacy of the proposed synthetic procedure to achieve the deposition of the Y_2O_3 phase in a very high dispersion state all over the ceria support.

With a view to confirming the spatial distribution of the rare earth dopant, X-EDS analyses were performed on the freshly prepared Y-containing nanomaterials. The chemical map registered for a single nanocube representative of the 20Y-CeO_2 NCs sample is illustrated in Fig. 4(b), where the signals for cerium and yttrium appear in red and blue, respectively. From them, it becomes evident that this latter chemical element chiefly accumulates on the surface of the ceria nanocubes, so that the outermost layers of both doped samples are

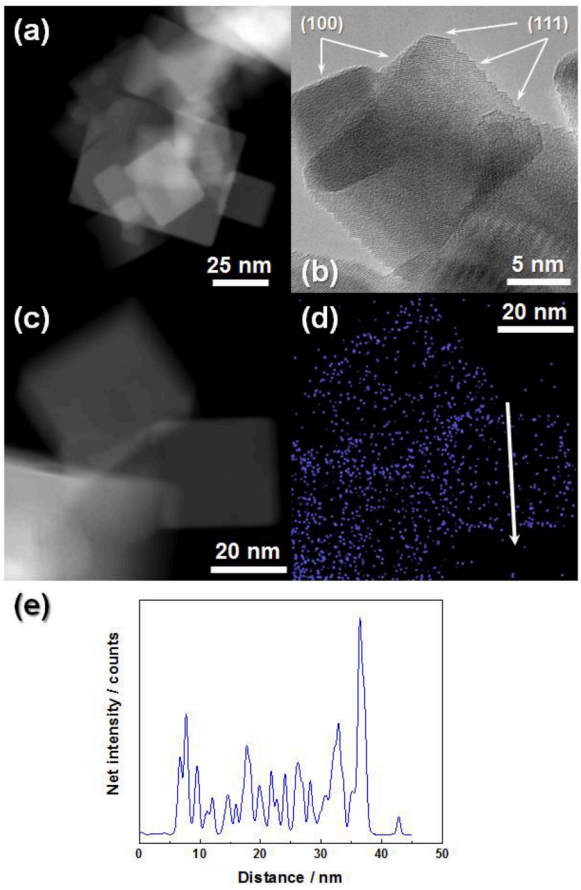

Fig. 5. Representative (S)TEM images of the 10Y-CeO_2 NCs-Ox600 sample: (a and c) HAADF-STEM images and (b) HRTEM image displaying the (111) nanofacets. (d) X-EDS map showing the distribution of yttrium (blue-coloured). (e) Intensity profile registered along the white arrow marked on (d).

exclusively composed of Y_2O_3. This oxide seems to form relatively uniform, epitaxially-grown, ultrathin surface layers, whose average thickness is roughly estimated to be in the range from 1 to 3 nm. As expected, the Y_2O_3 layer thickness is larger for the 20Y-CeO_2 NCs sample in comparison with its counterpart having a lower yttrium content. Additionally, the intensity profile of this chemical signal (see Fig. 4(c)) along the line perpendicular to the (100) surfaces shown in Fig. 4(b) clearly corroborates the details of the aforementioned spatial distribution for the rare earth dopant. One notes that the yttrium signal is markedly more intense just at the position of the very first crystallographic planes at the surfaces of the Y_2O_3-coated CeO_2 NCs. More to the interior of the nanoparticles, the signal intensity steeply drops but it does not reach a zero value, which means that this element is still detected although in much lower amounts, and then sharply increases again at the first planes of the opposite surface. This latter feature is attributable to and compatible with a complete coverage of the CeO_2 nanocubes by the Y_2O_3 phase, as has been previously pointed out.

At this point, it is worth noting a key issue regarding the unambiguous identification and characterisation of the highly dispersed Y-containing phases in the as-prepared nanostructured systems by means of HAADF-STEM. In this imaging mode the recorded intensity increases both with the atomic number (Z) of the elements present in the imaged area, following a $Z^{1.8}$-type dependence, and thickness. Accordingly, the discrimination of a lower intensity, few nanometre-thick, Y_2O_3 layer supported on a much higher intensity CeO_2 nanocube substrate becomes a major challenge. This problem is exacerbated because of the expected structural coherence between the two oxide components (i.e., CeO_2 and Y_2O_3), which display a cubic crystal lattice with rather similar cell

parameters (0.5411 nm for CeO_2 versus 0.5302 nm for Y_2O_3). A satisfactory solution can be only reached on the basis of data provided by complementary nanoanalytical techniques, such as the X-EDS chemical map collected in Fig. 4(b).

In order to gain a better insight into the evolution of their morphology, structure, and elemental distribution at the nanoscale, both freshly prepared Y-doped samples were further subjected to a couple of thermochemical ageing treatments consisting of heating at 600°C for 1 h under a 60 $cm^3 \cdot min^{-1}$ STP flow of O_2(5%)/He or H_2(5%)/Ar. Then, the resulting thermally aged nanomaterials were characterised by electron microscopy techniques. Similar results were found irrespective of the overall yttrium content in the samples, so that only those concerning the 10Y-CeO_2 NCs specimen will be hereinafter displayed and discussed for the sake of brevity.

Fig. 5(a) depicts a low magnification HAADF-STEM image recorded for the above material after applying the aforesaid oxidising treatment, which will be henceforth referred to as 10Y-CeO_2 NCs-Ox600. From this image, it becomes apparent that as a rule the oxidised nanoparticles largely retain a cubic-like shape. Nonetheless, the HRTEM image in Fig. 5(b) clearly reveals the presence at the corners of truncations related with (110) and (111) facets [39,52–54] and, much more importantly, of noticeable roughness on some surfaces of the nanocrystals. This latter feature, which exhibit a well-defined sawtooth-like or zigzagged shape when imaged down the appropriate zone axis, is specifically ascribable to (111) nanofacets with an average extent of approximately 1 nm and developed at the original location of (110) facets in the edges of the untreated sample. Such peculiar surface structure closely resembles to that previously reported by our research group for a bare ceria nanocubes sample submitted to an identical oxidation treatment [39,40,55]. Accordingly, the incorporation of the nanometre-thick yttria layer appears not to affect the surface restructuration of the CeO_2 NCs support imposed by the (111)-nanofaceting process induced by oxidation at intermediate temperatures (i.e., up to 600°C).

Fig. 5(d) illustrates the spatial distribution of the rare earth dopant in the 10Y-CeO_2 NCs-Ox600 sample. From this map, it is observed that, despite the applied oxidation treatment at 600°C, yttrium remains mostly concentrated at surface positions of the nanomaterial and as a relatively thin layer. Such observation is further corroborated from the corresponding intensity profile acquired for yttrium along the path marked on Fig. 5(d) and normal to the (100) facet of the cubic nanocrystal (see Fig. 5(e)). Again, a profile rather similarly shaped to that discussed above for the fresh nanomaterial is also obtained, thus allowing to exclude the formation of CeO_2-Y_2O_3 mixed oxide phases as a result of yttrium diffusion into the bulk of the CeO_2 nanocubes upon oxidation at temperatures of 600°C and below. This behaviour is just the expected one, since it is well-known that the diffusion of REE cations from a supported oxide phase into the CeO_2 lattice requires the presence of a significant amount of oxygen vacancies in this latter and thereby the application of thermochemical treatments under reducing atmosphere.

On the other hand, electron microscopy characterisation studies conducted on the sample 10Y-CeO_2 NCs-Red600, resulting from the reduction of the fresh 10Y-CeO_2 NCs material in H_2(5%)/Ar at a temperature of 600°C for 1 h, clearly evidence that this ageing treatment induces dramatic changes not only in the morphological features but also in the structure at nanoscale. Before discussing these results, however, it is noteworthy that immediately after applying the above thermochemical treatment the sample was submitted to a passivation protocol consisting of cooling down to -90°C under a 60 $cm^3 \cdot min^{-1}$ STP flow of pure He, switching to O_2(5%)/He at the same temperature, and then slowly warming up to room temperature. Such protocol was intended to prevent a very fast and uncontrolled re-oxidation of the reduced sample by its sudden contact with air during the storage and transport to the electron microscope.

At first sight, the most relevant and evident change observed for the 10Y-CeO_2 NCs-Red600 specimen in comparison with the untreated fresh sample concerns both the particle size and morphology. As revealed by the representative STEM image shown in Fig. 6(a), the thermal treatment at 600°C under reducing atmosphere leads to noticeable sintering of the starting cubic nanocrystals, which have now turned into larger crystals with a quite irregular shape bounded by a variety of crystallographic planes. Such sintering process may be favoured to some extent by the water release occurring because of the surface reduction of CeO_2. Furthermore, it should be highlighted that the reduction treatment is also accompanied by a restructuration of the nanocubes surface, which entails the development of the abovementioned (111)-nanofacets and confers the characteristic zigzagged appearance displayed in Fig. 6(b). Nonetheless, this (111)-nanofaceting process, now induced by mild reduction, seems to be more pronounced than that described for the sample 10Y-CeO_2 NCs-Ox600, thus leading to a larger extent of the nanofacets, which in some cases scale up to around 6 nm. Similarly, Fig. 6(b) also reveals an increase in the extent of the (111) facets associated with truncations at the corners of the cubes as compared to the 10Y-CeO_2 NCs-Ox600 sample. At this point, it is worth noting that these results are extremely interesting as they contradict the behaviour previously reported by Crozier et al. for pure CeO_2 nanocubes [56]. According to their work, the sawtooth like structure made up of adjoined low-energy (111) nanofacets flattens upon reduction treatment and transforms into a quite smooth (100) surface, which is able to better accommodate the corresponding oxygen vacancies due to its lower vacancy formation energy [20,57]. At first glance, our findings are apparently rather unexpected and surprising; however, they could be tentatively explained and understood on the basis of the presence of yttrium at surface and subsurface positions. It has been well established the ability of Y^{3+} to order the surface oxygen vacancies, which are created during the reduction treatment, in its vicinity [58]. Therefore, yttrium at surface level may accommodate and stabilise oxygen vacancies, thus hindering oxygen mobility and the conversion of the (111) nanofacets into a (100) surface.

Finally, X-EDS nanoanalyses were also performed on the 10Y-CeO_2 NCs-Red600 sample in order to determine the spatial distribution of yttrium, one of the resulting chemical maps being depicted in Fig. 6(d). As deduced from this figure, the REE dopant is still observed to concentrate mainly at the surface of the nanomaterial as a quite thin layer after applying the thermochemical treatment at 600°C under

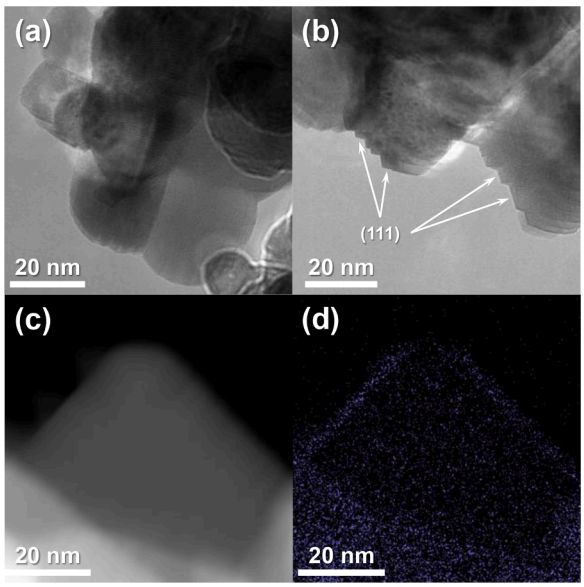

Fig. 6. Representative (S)TEM images of the 10Y-CeO_2 NCs-Red600 sample: (a and b) HRTEM images showing the (111) nanofacets. (c) HAADF-STEM image and (d) its corresponding X-EDS map displaying the distribution of yttrium (blue-coloured).

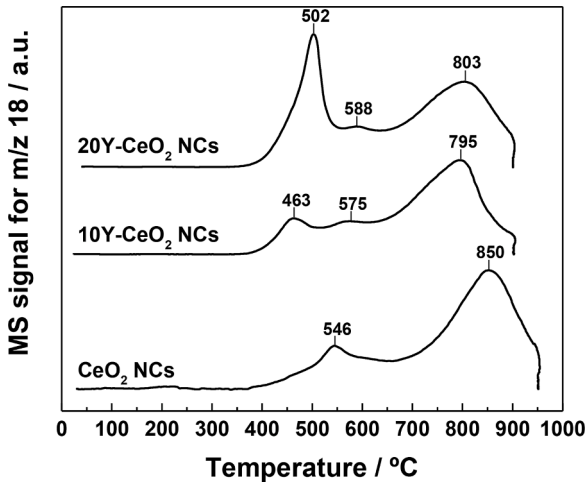

Fig. 7. Evolution of water (m/z = 18) during the H_2-TPR experiments performed on the freshly prepared CeO_2 NCs and XXY-CeO_2 NCs samples.

reducing atmosphere. Nonetheless, the thickness of the yttria surface layer apparently increases, thus suggesting a certain yttrium diffusion into the bulk of the ceria nanocrystal upon reduction, whose extent seems to be rather limited.

Additionally, the accumulation of yttrium in positions close to the surface of the nanocrystals even after the application of oxidation and reduction treatments at intermediate temperatures (i.e., up to 600°C) is a distinct feature, which may also expand the potential application of these yttria-coated ceria nanostructured materials as electrode in solid oxide fuel and electrolytic cells (SOFCs and SOECs, respectively). In this regard, the ultrathin, epitaxially-grown, yttria surface layers may act as an effective barrier to limit both the sintering of the ceria nanocrystals and the undesirable diffusion at operating temperatures of cerium in the zirconia-based electrolytes typically employed in these devices.

3.3. Redox characterisation

As previously commented, in recent years a number of works have underlined the key role played by the redox properties of CeO_2 and related materials in the CO_2 activation process ([27,35,37] and references therein), which is generally agreed to follow a mechanism involving oxygen vacancies. Furthermore, on the basis of our starting hypothesis, surface modifications imposed by the incorporation of Y_2O_3 as ultrathin layers are expected to markedly influence the redox behaviour of the resulting CeO_2-based nanostructured materials. Accordingly, TPR experiments under flowing H_2(5%)/Ar were accomplished on both the bare and Y_2O_3-coated CeO_2 NCs samples with a view to fully characterising such relevant properties. The obtained TPR results are collected in Fig. 7 as water evolution curves, a complete consistency with the corresponding hydrogen consumption profiles being found for all three nanomaterials. Therefore, the different events observed in the former curves are all unambiguously connected with abstraction of lattice oxygen from the oxide samples by hydrogen.

Regarding the reference CeO_2 NCs, its TPR profile features the typical bimodal shape widely reported in the literature for pure ceria in the form of both nanostructured and conventional high surface area powders [9,59–61]. The low temperature peak located at around 546°C has been traditionally ascribed to surface reduction of CeO_2, whereas the much more intense and very broad band peaked at 850°C has been associated with bulk oxide reduction.

As far as the yttria-coated samples are concerned, Fig. 7 clearly evidences that the incorporation of Y_2O_3 as ultrathin layers on the well-defined crystallographic surfaces of the pristine CeO_2 NCs brings about noticeable changes in the TPR profile of this latter nanomaterial. Thus, the most prominent modification affects the low temperature reduction peak, which undergoes not only an intensity increase but also a significant shift of its position to lower temperatures. Both observations are in good agreement with the expected improvement in the reducibility at low temperature of the bare CeO_2 NCs as a consequence of their controlled surface doping with yttrium, despite the water evolution signal starts at the same temperature (i.e., around 370°C) for all three nanostructured materials. Furthermore, the intensity of the first reduction peak markedly increases with yttrium loading, even becoming much greater than the high temperature band for the 20Y-CeO_2 NCs specimen. By contrast, an opposite trend is observed for the displacement of this low temperature signal relative to its position for the reference CeO_2 NCs, which is smaller for the sample with the higher dopant content (i.e., 44°C for 20Y-CeO_2 NCs *vs* 83°C for 10Y-CeO_2 NCs). In this connection, similar results have been previously reported by our research group for a series of CeO_2 NCs samples modified with increasing praseodymium concentrations in the range from 5 to 20 mol. % [43], although in this case the rare earth dopant was homogeneously distributed throughout the entire nanomaterials at both surface and bulk levels, and not only concentrated at their outermost surface layers. All the above changes involving the first peak are also accompanied by a decrease in the intensity of the bulk reduction band, being obviously more pronounced for 20Y-CeO_2 NCs. This fact would suggest that lattice oxygen might be involved to some extent in the reduction events occurring at low temperature for the Y-doped samples.

Summarising the whole set of results derived from TPR experiments, the proposed synthetic strategy based on surface doping of crystallographically well-defined CeO_2 nanocubes with Y_2O_3 was revealed as a successful approach not only to enhance the reducibility of the ceria substrate at low temperature, but also to promote the oxide ion mobility in the fluorite-type lattice due to the introduction of additional oxygen vacancies.

3.4. Surface basicity characterisation

Surface basic features of solid catalysts are closely related to CO_2 adsorption, which is a mandatory step prior to activation of this highly stable molecule. Moreover, the slightly basic surface of the pristine ceria nanocubes is expected to undergo major modifications as a result of the deposition of the ultrathin Y_2O_3 layers. Consequently, it becomes apparent the interest of carefully characterising the surface basicity of the prepared nanostructured materials with a view to their potential incorporation as support or even promoter in catalysts formulations for CO_2 valorisation. For such a purpose, TPD-MS and volumetric adsorption experiments were performed on both the fresh uncoated and yttria-coated samples. At this point, it is worth recalling that CO_2 has been traditionally employed as a probe molecule to analyse the surface basic properties of a number of oxides, including those of rare earths, with interest in heterogeneous catalysis [18,62–64]. Despite some quantitative information could be derived from TPD-MS assays by integration of the registered traces, it should be highlighted that these studies were essentially aimed at evaluating the relative thermal stability of the pre-adsorbed CO_2 species and thereby the strength of the different basic sites present in the nanomaterials surface. On the contrary, more accurate quantitative information about both reversible and irreversible forms of adsorbed CO_2 was obtained from complementary volumetric adsorption experiments at 35°C.

Prior to starting the TPD-MS experiments, the nanostructured oxide samples were subjected to a cleaning pretreatment under flowing O_2(5%)/He at 350°C for 1 h. Such temperature was selected in order not to exceed the calcination temperature employed in the preparation of the yttria-containing nanomaterials, thus avoiding additional morphological and nanostructural modifications. Nevertheless, these cleaning conditions cannot ensure a complete removal of carbonate species present in the samples, especially of those strongly chemisorbed, which in turn leads to the appearance of a set of desorption peaks and bands above 350°C in the TPD traces and seriously hinders their appropriate

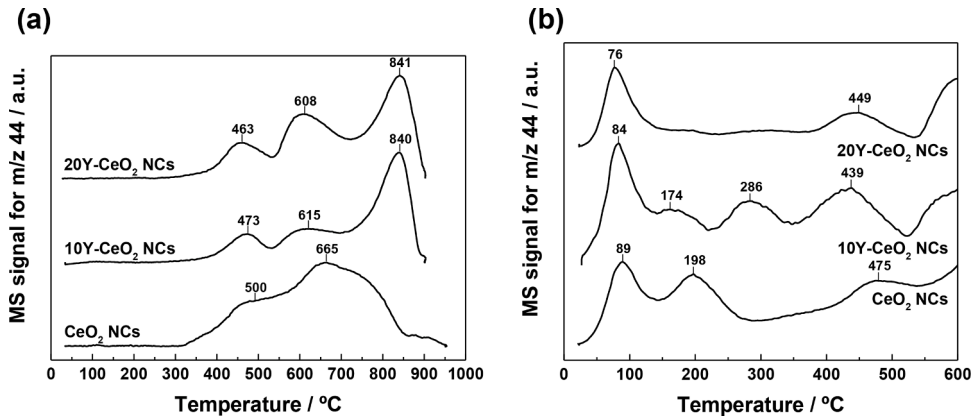

Fig. 8. TPD-MS profiles of CO_2 ($m/z = 44$) desorption from the freshly prepared CeO_2 NCs and XXY-CeO_2 NCs samples, without any CO_2 treatment (a) and after CO_2 adsorption at room temperature. Prior to these experiments, all the oxide samples were subjected to a cleaning routine in flowing O_2(5%)/He at 350°C for 1 h. MS signals have been referred to 1 m^2 of surface area of the nanomaterials.

Table 2
Amounts of chemisorbed CO_2 as estimated by integration of the corresponding TPD profiles.

Sample	Total amount of desorbed CO_2 [a] /		Amount of retained CO_2 [b] /	
	$\mu mol \cdot g^{-1}$	$molec \cdot nm^{-2}$	$\mu mol \cdot g^{-1}$	$molec \cdot nm^{-2}$
CeO_2 NCs	12.75	0.37	8.31	0.24
10Y-CeO_2 NCs	27.92	0.94	21.68	0.73
20Y-CeO_2 NCs	27.12	0.87	23.32	0.75

[a] As determined by integration of the TPD diagrams depicted in Fig. 8(b) for the samples submitted to the cleaning protocol and further treated with flowing CO_2 ($P_{CO_2} = 1$ atm) at 25°C for 1 h.

[b] As determined by integration of the TPD diagrams depicted in Fig. 8(a) for the samples submitted to the cleaning protocol, without any further treatment.

interpretation. With a view to evaluating this contribution of the CO_2 retained by the ceria-based nanomaterials after applying the oxidising pretreatment, blank TPD experiments were also performed on the oxide samples submitted to the cleaning protocol, without any further treatment. The recorded diagrams are collected in Fig. 8(a), while the quantitative data resulting from their integration are gathered in the fourth and fifth columns of Table 2.

As can be seen, the CO_2 evolution profile for the pretreated bare ceria nanocubes only exhibits a very broad and medium intensity band spanning from around 300°C up to 850°C and peaked at 665°C, with a clearly visible shoulder located at roughly 500°C. These features are compatible with the desorption of a variety of hydrogencarbonate, carbonate, and even formate and carboxylate species with different thermal stability, both as surface and bulk forms [65–68]. In fact, the TPD curve can be deconvoluted into two Gaussian peaks centred at ca. 475 and 685°C, this latter being much more intense and broader than the former and likely attributable to strongly bound bulk carbonate species. After yttria incorporation, CO_2 evolution signals are markedly different and become three-modal with a series of not well-resolved and increasingly intense peaks centred at 460-475, 605-615, and 840°C. Before discussing their tentative assignment, it is worth mentioning that such features are essentially connected with the surface yttria phases, in line with the homogeneity and high dispersion of these latter as deduced from electron microscopy studies. Indeed, ultrathin yttria layers appear to largely limit atmospheric CO_2 diffusion into ceria lattice and thereby the formation of bulk carbonate species, as inferred from the severe decrease in the contribution of the broad band peaking at 665°C in the blank TPD curves for both yttria-coated samples as compared to that for the raw CeO_2 NCs. The origin of the above three peaks is not clear; however, they could be ascribed to the thermal desorption of several carbonate species formed on the samples surface due to their exposure to air during storage and handling and not decomposed in the cleaning pretreatment. According to thermal stability studies performed by FT-IR spectroscopy on commercial Y_2O_3 powders after exposure to a static atmosphere of 10 mbar CO_2 [69] (i.e., experimental conditions much closer to the storage and handling of the samples than those employed in typical experiments carried out at atmospheric pressure), hydrogencarbonate species (both monodentate and bidentate) decompose at temperatures below 200°C, so that their presence in the yttria-doped nanomaterials can be discarded after the cleaning pretreatment. By contrast, bridged carbonates are expected to be the remaining major species in the pretreated samples, and they are progressively converted into polydentate carbonates upon further heating up to 600°C during the blank TPD experiments. Since polydentate carbonates are the only stable species above this temperature, the more intense and better defined peak appearing at around 840°C in the traces for both coated samples could be attributed to CO_2 release from their thermal decomposition. Summarising these observations, a complete removal of the different CO_2 chemisorbed species on Y_2O_3 requires a cleaning pretreatment under oxidising atmosphere at temperatures above 600°C, much higher than that applied in the present work.

Concerning quantitative data derived from integration of the blank TPD profiles in Fig. 8(a) (see fourth and fifth columns in Table 2), it becomes clear that the amount of the strongest chemisorbed CO_2 forms is non-negligible for all three nanostructured materials. Furthermore, it drastically increases after yttria deposition from 8.31 $\mu mol \cdot g^{-1}$ and 0.24 $molec \cdot nm^{-2}$ for CeO_2 NCs to 21.68 $\mu mol \cdot g^{-1}$ and 0.73 $molec \cdot nm^{-2}$ for 10Y-CeO_2 NCs, the effect being much more moderate as the thickness of the surface layer is raised (i.e., 23.32 $\mu mol \cdot g^{-1}$ and 0.75 $molec \cdot nm^{-2}$ for 20Y-CeO_2 NCs). Overall, these results corroborate the presence in the coated samples of a higher amount of strongly bound carbonate species, which are mostly associated with the ultrathin yttria layers.

Obtained results from the TPD-MS experiments after CO_2 adsorption at room temperature are summarised in Fig. 8(b) and Table 2. Before discussing and analysing them, it should be borne in mind that the oxide samples were submitted to the aforementioned cleaning pretreatment in O_2(5%)/He at 350°C, then they were exposed to a pure CO_2 flow at 25°C for 1 h, and finally flushed with pure Ar at the same temperature for 1 h. Therefore, since this latter purging removes physically adsorbed CO_2 species, it becomes clear that data reported in Table 2 and Fig. 8(b) chiefly account for those irreversibly adsorbed CO_2 forms. In order to make meaningful comparisons, the MS signals have been all normalised by the specific surface area values of the corresponding ceria-based nanomaterials.

First, it is worth mentioning that above 600°C the TPD diagrams are rather similarly shaped to those recorded during the blank experiments without previous CO_2 adsorption, particularly for the CeO_2 NCs sample.

Accordingly, these curves have been plotted from room temperature to 600°C in Fig. 8(b) for the sake of comparison. Therefore, it may be concluded that most of the CO_2 retained by the nanostructured oxides is evolved at low and intermediate temperatures (i.e., below 500°C), which is a quite interesting property with a view to the potential incorporation of these ceria-based materials in the formulations of catalysts for CO_2 valorisation at mild temperatures.

The TPD trace for the bare CeO_2 NCs is dominated by two partially overlapped major desorption peaks centred at around 89 and 198°C, the former being slightly more intense and sharper than the latter, followed by a tail extending up to 300°C and then a poorly resolved and broad band with a maximum at 475°C. Both the position and intensity of the low temperature peaks are in good agreement with the results previously reported in the literature for TPD experiments performed on ceria nanocubes after CO_2 adsorption at 50°C [70]. Furthermore, Wu et al. employed a combination of TPD-MS and FT-IR spectroscopy to unveil the nature of the different species formed on the surface of ceria nanocubes, among other nanoshapes, as a result of CO_2 adsorption at room temperature. In accordance to their findings, the two main peaks observed in the CO_2 evolution profile for CeO_2 NCs are likely ascribed to the desorption of hydrogencarbonate species, which thermally decompose at temperatures below 200°C [68]. In this connection, it should be noted that the presence of hydrogencarbonate species in the pretreated sample cannot be ruled out providing that trace impurities of water are present in the pure CO_2 stream used in the pre-adsorption stage. These water molecules adsorb on nanomaterial surface at room temperature to yield hydroxyl groups, which subsequently chemisorb CO_2 in the form of hydrogencarbonate [68]. Finally, it is also noteworthy that the aforesaid major desorption features occur at temperatures slightly higher than those observed for ceria nanooctahedra (enclosed by (111) facets) [68, 70] and high surface area bulk ceria [71], thus suggesting that basic surface sites on CeO_2 NCs (essentially bounded by (100) planes) are somewhat stronger. Such a behaviour has been partly attributed to a higher concentration of oxygen vacancies on CeO_2 NCs surface, since the presence of these defects has been associated with an enhancement in the surface basicity of this lanthanoid oxide [72]. All these conclusions are also consistent with recent theoretical and experimental works about CO_2 adsorption on (111) and (100) ceria surfaces [73–75].

As can be seen in Fig. 8(b), the deposition of yttria as ultrathin layers on the crystallographically well-defined surfaces of ceria nanocubes dramatically modifies the CO_2 desorption profiles. Thus, the traces for 10Y-CeO_2 NCs and 20Y-CeO_2 NCs samples display as most prominent feature a desorption peak located at around 80°C with a tail up to 140°C, accompanied by a set of three not well-resolved and overlapping bands centred at approximately 170, 285, and 445°C. The position of the major peak slightly shifts to lower temperatures in comparison with that observed for the pristine CeO_2 NCs (i.e., ca. 89°C), thereby suggesting a moderate decrease in the strength of the weakest basic surface centres for both coated samples. Another aspect worth highlighting is the marked decline of intensity for the desorption features as the Y content increases. Indeed, the relatively broad bands peaking at 150 and 285°C in the curve for the 10Y-CeO_2 NCs sample almost vanish in the profile for its counterpart containing a 20 at.% Y, whereas that centred at 445°C undergoes a noticeable decrease in intensity. A clear identification of the origin of the above desorption features is a quite complex task; however, it may be concluded that the modification of ceria nanocubes by depositing ultrathin yttria layers induces the creation of a variety of basic surface centres with different strength.

Regarding the quantitative data shown in Table 2, there are some aspects that should be commented on. First, the total amount of desorbed CO_2 reported in the second and third columns of the above table clearly confirms that the yttria-coated samples not only exhibit a more varied basicity, but also a higher density of basic surface sites. Moreover, the influence of the yttria loading, and thereby of the layer thickness, on both the concentration and relative strength (i.e., thermal stability) of the basic centres on the samples surface is also noticeable. Thus, from

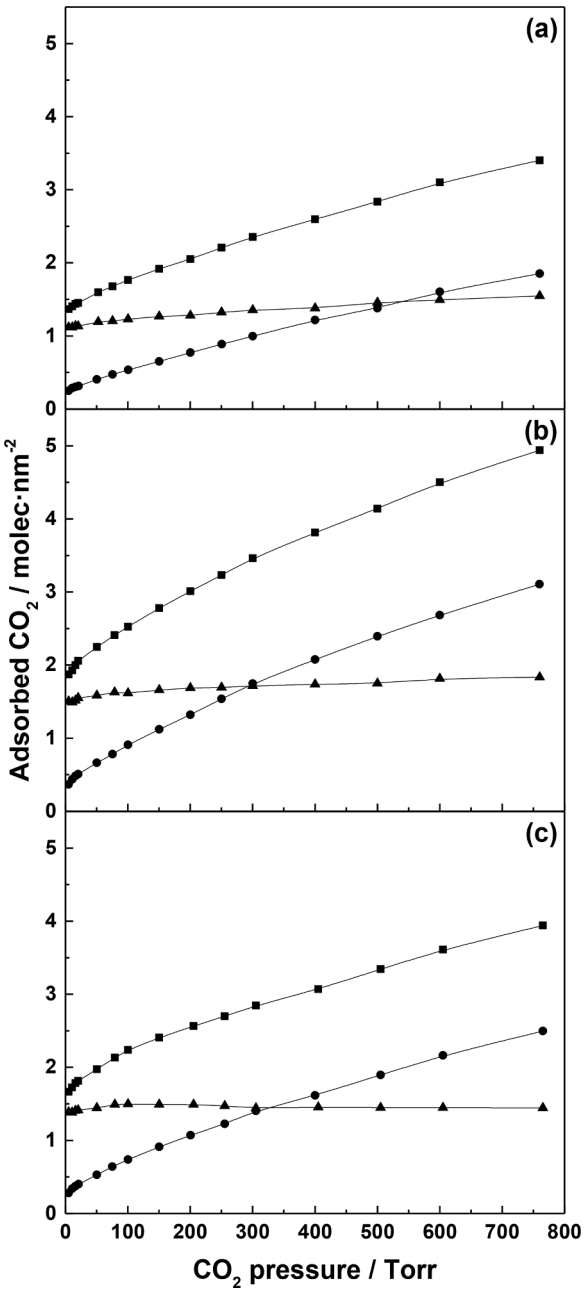

Fig. 9. First (■) and second (●) CO_2 volumetric chemisorption isotherms registered at 35°C on CeO_2 NCs (a), 10Y-CeO_2 NCs (b), and 20Y-CeO_2 NCs (c) samples. Irreversible adsorption data (▲) as estimated from the difference between the first and second isotherms.

Table 2 it also becomes apparent that the higher the yttria content and layer thickness, the lower the surface concentration of chemisorbed CO_2 and the higher the amount of CO_2 retained by the sample after the cleaning pretreatment. Finally, the strongly bound forms also account for a significant fraction of the total amount of desorbed CO_2, as inferred from the data collected in the fourth and fifth columns of Table 2.

In order to complement the information provided by the TPD-MS study, additional CO_2 volumetric chemisorption experiments were also performed on both the uncoated and yttria-coated nanostructured materials. In this connection, two consecutive isotherms at 35°C separated by an evacuation treatment at the same temperature for 1 h were registered. The resulting isotherms for each of the samples are plotted in Fig. 9. Moreover, adsorption data as calculated from the point-to-point difference between the first and second experimental isotherms have

Table 3
Total, reversible, and irreversible amounts of CO_2 adsorbed on the CeO_2 NCs and XXY-CeO_2 NCs samples, as estimated from volumetric adsorption experiments at 35°C.

Sample	Total adsorbed CO_2 [a] /		Reversibly adsorbed CO_2 [b] /		Irreversibly adsorbed CO_2 [c] /		Correctedamount ofirreversiblyadsorbedCO_2 [d] /	
	$mmol{\cdot}g^{-1}$	$molec{\cdot}nm^{-2}$	$mmol{\cdot}g^{-1}$	$molec{\cdot}nm^{-2}$	$mmol{\cdot}g^{-1}$	$molec{\cdot}nm^{-2}$	$mmol{\cdot}g^{-1}$	$molec{\cdot}nm^{-2}$
CeO_2 NCs	0.1187	3.40	0.0647	1.85	0.0540	1.55	0.0623	1.79
10Y-CeO_2 NCs	0.1469	4.94	0.0924	3.11	0.0545	1.83	0.0762	2.56
20Y-CeO_2 NCs	0.1229	3.94	0.0779	2.50	0.0450	1.44	0.0683	2.19

[a] As determined from the first isotherm ($P_{CO_2} = 760$ Torr).
[b] As determined from the second isotherm ($P_{CO_2} = 760$ Torr).
[c] As determined from the difference between the amounts of total (second and third columns) and reversibly (fourth and fifth columns) adsorbed CO_2 ($P_{CO_2} = 760$ Torr).
[d] As determined by the addition to the sixth and seventh columns of the amounts of CO_2 retained by the oxide samples after applying the cleaning protocol in O_2(5%)/He at 350°C for 1 h (fourth and fifth columns in Table 2).

been also included in the above figure. From this set of data, the total, reversible, and irreversible amounts of adsorbed CO_2 were estimated at a CO_2 pressure of 760 Torr, the obtained values being gathered in Table 3. The two last columns in this table accounts for the amounts of irreversibly adsorbed CO_2 resulting from the correction of those data reported in the two previous columns by the amounts of CO_2 not removed from the oxide samples during the application of the cleaning routine in O_2(5%)/He at 350°C for 1 h (fourth and fifth columns in Table 2).

As deduced from Fig. 9 and Table 3, the volumetric chemisorption data corroborate the previously commented effect of the ultrathin yttria surface layers on the CO_2 adsorption capacity of the bare ceria nanocubes. Such an effect is more pronounced on the reversibly chemisorbed CO_2, 0.0924 $mmol{\cdot}g^{-1}$ and 3.11 $molec{\cdot}nm^{-2}$ for 10Y-CeO_2 NCs in comparison with 0.0647 $mmol{\cdot}g^{-1}$ and 1.85 $molec{\cdot}nm^{-2}$ for CeO_2 NCs. Although not so marked, the influence of yttria surface doping on the amount of irreversibly adsorbed CO_2 species is also noticeable, 0.0762 $mmol{\cdot}g^{-1}$ and 2.56 $molec{\cdot}nm^{-2}$ for 10Y-CeO_2 NCs against 0.0623 $mmol{\cdot}g^{-1}$ and 1.79 $molec{\cdot}nm^{-2}$ for the pristine ceria substrate.

Concerning the influence of the thickness of the yttria surface layer, from the results reported in Fig. 9 and Table 3 it becomes apparent that the effect on the amount of both reversibly and irreversibly adsorbed CO_2 forms is stronger on the 10Y-CeO_2 NCs sample and slightly lower for its counterpart containing a 20 at.% Y loading. Accordingly, the thickness of the yttria layer epitaxially grown on the crystallographically well-defined facets of ceria nanocubes should be carefully adjust in order to achieve the surface basicity features (i.e., both density and relative strength of basic surface centres) required for a given CO_2 valorisation reaction.

4. Conclusions

Aimed at advancing in the rational design of more efficient catalysts for the valorisation of CO_2 into valuable feedstock molecules, we have devised a novel synthetic strategy to prepare ceria-based nanostructured materials with enhanced adsorption and activation properties towards this acidic and highly stable molecule. Our strategy relies on tailoring both the acid-base and redox surface features, which play a pivotal role in CO_2 adsorption and activation, of nanoshaped ceria by their coating with nanometre-thick, epitaxially-grown, yttria layers. Accordingly, starting from ceria nanocubes prepared by a hydrothermal method, ultrathin yttria layers equivalent to 10 and 20 at.% yttrium nominal loadings were deposited by a facile, surfactant-free, controlled chemical precipitation procedure. The whole set of results derived from the combined application of several characterisation techniques to the as-synthesised nanomaterials has allowed us to draw the following main conclusions:

1 Nanostructural and nanoanalytical studies performed by electron microscopy confirmed that the proposed synthetic approach successfully led to the deposition of the yttria phase in a highly dispersed state, forming few nanometre-thick layers by epitaxial growth on the crystallographically well-defined facets of the ceria nanocubes. Furthermore, these analyses also revealed that yttrium mostly remained concentrated at surface positions after applying thermochemical treatments at intermediate temperatures (i.e., up to 600°C) under both oxidising and reducing atmosphere.
2 The prepared yttria-doped nanomaterials displayed an improved reducibility, particularly in the low temperature range, as compared to that observed for the bare ceria nanocubes. This feature is considered as essential to achieve a suitable CO_2 activation at mild temperatures, which follows an oxygen vacancy-assisted mechanism and is thereby closely linked to the surface reducibility of the solid.
3 Surface yttria doping also brought about remarkable changes in the surface basicity of the pristine ceria nanocubes. Thus, as revealed by volumetric adsorption measurements, yttria-coated samples exhibited a greater CO_2 adsorption capacity, especially of those reversible forms. Additionally, TPD-CO_2 experiments clearly proved the presence in these nanomaterials of a higher number of basic surface centres with a broadly varied range of strength.
4 Controlling the thickness of the yttria surface layer enables to modulate the above effects on the surface basicity and reducibility of the nanostructured ceria substrate, and thereby its ability to adsorb and activate the CO_2 molecule.

To summarise, the proposed synthetic strategy paves the way toward a rational design of novel, high performance, ceria-based nanostructured catalysts for CO_2 valorisation by gaseous phase reactions under mild conditions.

Author statement

Adrián Barroso Bogeat: Conceptualization, Methodology, Investigation, Writing-Original draft preparation, Writing-Reviewing and Editing, Visualization.
Ginesa Blanco: Conceptualization, Methodology, Investigation, Writing-Reviewing and Editing, Supervision.
José María Pintado: Conceptualization, Methodology, Investigation, Writing-Reviewing and Editing, Supervision.
Daniel Goma: Investigation, Visualization.
José Juan Calvino Gámez: Conceptualization, Resources, Supervision.

Declaration of Competing Interest

The authors declare that they have no known competing financial interests or personal relationships that could have appeared to influence the work reported in this paper.

Acknowledgements

Financial support from the Spanish Ministry of Science and

Innovation and FEDER Program of EU (project MAT2017-87579-R), and Junta de Andalucía (groups FQM-110 and FQM-334) is gratefully acknowledged. Adrián Barroso Bogeat thanks support from "Juan de la Cierva-Formación" Fellowship Program of the Spanish Ministry of Science and Innovation (FJCI-2015-25999) and from the University of Cádiz through a postdoctoral contract. Electron microscopy data were acquired using the equipment at the DME-UCA node of the ELECMI Spanish Unique Infrastructure for Electron Microscopy of Materials.

References

[1] A. Trovarelli, Catalytic properties of ceria and CeO2-Containing materials, Catal. Rev. - Sci. Eng. 38 (1996) 439–520, https://doi.org/10.1080/01614949608006464.
[2] A. Trovarelli, C. de Leitenburg, M. Boaro, G. Dolcetti, The utilization of ceria in industrial catalysis, Catal. Today. 50 (1999) 353–367, https://doi.org/10.1016/S0920-5861(98)00515-X.
[3] A. Trovarelli, Catalysis by Ceria and Related Materials, 1st ed., Imperial College Press, London, 2002 https://doi.org/10.1142/p249.
[4] A. Trovarelli, P. Fornasiero (Eds.), Catalysis by Ceria and Related Materials, 2nd ed., Imperial College Press, London, 2013 https://doi.org/10.1142/p870.
[5] T. Montini, M. Melchionna, M. Monai, P. Fornasiero, Fundamentals and Catalytic Applications of CeO2-Based Materials, Chem. Rev. 116 (2016) 5987–6041, https://doi.org/10.1021/acs.chemrev.5b00603.
[6] A. Trovarelli, Structural and Oxygen Storage/Release Properties of CeO2-Based Solid Solutions, Comments Inorg. Chem. A J. Crit. Discuss. Curr. Lit. 20 (1999) 263–284, https://doi.org/10.1080/02603599908021446.
[7] D. Duprez, C. Descorme, Oxygen Storage/Redox Capacity and Related Phenomena on Ceria-Based Catalysts, in: A. Trovarelli (Ed.), Catal. by Ceria Relat. Mater, 1st ed., Imperial College Press, London, 2002, pp. 243–280, https://doi.org/10.1142/9781860949654_0007.
[8] R. Di Monte, J. Kašpar, On the role of oxygen storage in three-way catalysis, Top. Catal. 28 (2004) 47–58, https://doi.org/10.1023/b:toca.0000024333.08447.f7.
[9] F. Giordano, A. Trovarelli, C. de Leitenburg, M. Giona, A Model for the Temperature-Programmed Reduction of Low and High Surface Area Ceria, J. Catal. 193 (2000) 273–282, https://doi.org/10.1006/jcat.2000.2900.
[10] E. Aneggi, M. Boaro, C. de Leitenburg, G. Dolcetti, A. Trovarelli, Insights into the redox properties of ceria-based oxides and their implications in catalysis, J. Alloys Compd. 408–412 (2006) 1096–1102, https://doi.org/10.1016/j.jallcom.2004.12.113.
[11] F. Giordano, A. Trovarelli, C. de Leitenburg, G. Dolcetti, M. Giona, Some insight into the effects of oxygen diffusion in the reduction kinetics of ceria, Ind. Eng. Chem. Res. 40 (2001) 4828–4835, https://doi.org/10.1021/ie010105q.
[12] C. Sun, H. Li, L. Chen, Nanostructured ceria-based materials: synthesis, properties, and applications, Energy Environ. Sci. 5 (2012) 8475–8505, https://doi.org/10.1039/c2ee22310d.
[13] J.M. Gatica, D.M. Gómez, J.C. Hernández-Garrido, J.J. Calvino, G.A. Cifredo, H. Vidal, Experimental evidences of the relationship between reducibility and micro- and nanostructure in commercial high surface area ceria, Appl. Catal. A Gen. 479 (2014) 35–44, https://doi.org/10.1016/j.apcata.2014.04.030.
[14] J.J. Delgado, E. del Río, X. Chen, G. Blanco, J.M. Pintado, S. Bernal, J.J. Calvino, Understanding Ceria-Based Catalytic Materials: An Overview of Recent Progress, in: A. Trovarelli, P. Fornasiero (Eds.), Catal. by Ceria Relat. Mater, 2nd ed., Imperial College Press, London, 2013, pp. 47–138, https://doi.org/10.1142/9781848169647_0002.
[15] M. Capdevila-Cortada, G. Vilé, D. Teschner, J. Pérez-Ramírez, N. López, Reactivity descriptors for ceria in catalysis, Appl. Catal. B Environ. 197 (2016) 299–312, https://doi.org/10.1016/j.apcatb.2016.02.035.
[16] M.P. Rosynek, Catalytic Properties of Rare Earth Oxides, Catal. Rev. Sci. Engeneering. 16 (1977) 111–154, https://doi.org/10.1080/03602457708079635.
[17] S. Bernal, G. Blanco, J.J. Calvino, J.A. Pérez Omil, J.M. Pintado, Some major aspects of the chemical behavior of rare earth oxides: An overview, J. Alloys Compd. 408–412 (2006) 496–502, https://doi.org/10.1016/j.jallcom.2004.12.090.
[18] S. Sato, R. Takahashi, M. Kobune, H. Gotoh, Basic properties of rare earth oxides, Appl. Catal. A Gen. 356 (2009) 57–63, https://doi.org/10.1016/j.apcata.2008.12.019.
[19] D.R. Mullins, The surface chemistry of cerium oxide, Surf. Sci. Rep. 70 (2015) 42–85, https://doi.org/10.1016/j.surfrep.2014.12.001.
[20] A. Trovarelli, J. Llorca, Ceria Catalysts at Nanoscale: How Do Crystal Shapes Shape Catalysis? ACS Catal 7 (2017) 4716–4735, https://doi.org/10.1021/acscatal.7b01246.
[21] L. Vivier, D. Duprez, Ceria-based solid catalysts for organic chemistry, ChemSusChem 3 (2010) 654–678, https://doi.org/10.1002/cssc.201000054.
[22] M. Utiyama, H. Hattori, K. Tanabe, Exchange reaction of methane with deuterium over solid base catalysts, J. Catal. 53 (1978) 237–242, https://doi.org/10.1016/0021-9517(78)90071-4.
[23] V.R. Choudhary, V.H. Rane, Acidity/basicity of rare-earth oxides and their catalytic activity in oxidative coupling of methane to C2-hydrocarbons, J. Catal. 130 (1991) 411–422, https://doi.org/10.1016/0021-9517(91)90124-M.
[24] J.S.J. Hargreaves, G.J. Hutchings, R.W. Joyner, S.H. Taylor, A study of the methane-deuterium exchange reaction over a range of metal oxides, Appl. Catal. A Gen. 227 (2002) 191–200, https://doi.org/10.1016/S0926-860X(01)00935-8.
[25] S. Bernal, J.J. Calvino, M.A. Cauqui, J.M. Gatica, C. Larese, J.A. Pérez Omil, J. M. Pintado, Some recent results on metal/support interaction effects in NM/CeO2 (NM: noble metal) catalysts, Catal. Today. 50 (1999) 175–206, https://doi.org/10.1016/S0920-5861(98)00503-3.
[26] S. Bernal, J.J. Calvino, M.A. Cauqui, J.M. Gatica, C. López Cartes, J.A. Pérez Omil, J.M. Pintado, Some contributions of electron microscopy to the characterisation of the strong metal-support interaction effect, Catal. Today. 77 (2003) 385–406, https://doi.org/10.1016/S0920-5861(02)00382-6.
[27] M. Boaro, S. Colussi, A. Trovarelli, Ceria-based materials in hydrogenation and reforming reactions for CO2 valorization, Front. Chem. 7 (2019) 28, https://doi.org/10.3389/fchem.2019.00028.
[28] J.A. Rodriguez, D.C. Grinter, Z. Liu, R.M. Palomino, S.D. Senanayake, Ceria-based model catalysts: fundamental studies on the importance of the metal-ceria interface in CO oxidation, the water-gas shift, CO2 hydrogenation, and methane and alcohol reforming, Chem. Soc. Rev. 46 (2017) 1824–1841, https://doi.org/10.1039/c6cs00863a.
[29] T.H. Etsell, S.N. Flengas, The electrical properties of solid oxide electrolytes, Chem. Rev. 70 (1970) 339–376, https://doi.org/10.1021/cr60265a003.
[30] C. Artini, Rare-Earth-Doped Ceria Systems and Their Performance as Solid Electrolytes: A Puzzling Tangle of Structural Issues at the Average and Local Scale, Inorg. Chem. 57 (2018) 13047–13062, https://doi.org/10.1021/acs.inorgchem.8b02131.
[31] M. Coduri, S. Checchia, M. Longhi, D. Ceresoli, M. Scavini, Rare Earth Doped Ceria: The Complex Connection Between Structure and Properties, Front. Chem. 6 (2018) 526, https://doi.org/10.3389/fchem.2018.00526.
[32] E. Aneggi, D. Wiater, C. de Leitenburg, J. Llorca, A. Trovarelli, Shape-dependent activity of ceria in soot combustion, ACS Catal 4 (2014) 172–181, https://doi.org/10.1021/cs400850r.
[33] U. Castanet, C. Feral-Martin, A. Demourgues, R.L. Neale, D.C. Sayle, F. Caddeo, J. M. Flitcroft, R. Caygill, B.J. Pointon, M. Molinari, J. Majimel, Controlling the {111}/{110} Surface Ratio of Cuboidal Ceria Nanoparticles, ACS Appl. Mater. Interfaces. 11 (2019) 11384–11390, https://doi.org/10.1021/acsami.8b21667.
[34] Y. Li, W. Shen, Morphology-dependent nanocatalysts: Rod-shaped oxides, Chem. Soc. Rev. 43 (2014) 1543–1574, https://doi.org/10.1039/c3cs60296f.
[35] Y. Ma, W. Gao, Z. Zhang, S. Zhang, Z. Tian, Y. Liu, J.C. Ho, Y. Qu, Regulating the surface of nanoceria and its applications in heterogeneous catalysis, Surf. Sci. Rep. 73 (2018) 1–36, https://doi.org/10.1016/j.surfrep.2018.02.001.
[36] M. Mikkelsen, M. Jørgensen, F.C. Krebs, The teraton challenge. A review of fixation and transformation of carbon dioxide, Energy Environ. Sci. 3 (2010) 43–81, https://doi.org/10.1039/B912904A.
[37] K. Chang, H. Zhang, M. Cheng, Q. Lu, Application of Ceria in CO2 Conversion Catalysis, ACS Catal 10 (2020) 613–631, https://doi.org/10.1021/acscatal.9b03935.
[38] H.-X. Mai, L.-D. Sun, Y.-W. Zhang, R. Si, W. Feng, H.-P. Zhang, H.-C. Liu, C.-H. Yan, Shape-selective synthesis and oxygen storage behavior of ceria nanopolyhedra, nanorods, and nanocubes, J. Phys. Chem. B. 109 (2005) 24380–24385, https://doi.org/10.1021/jp055584b.
[39] M. Tinoco, S. Fernandez-Garcia, M. Lopez-Haro, A.B. Hungria, X. Chen, G. Blanco, J.A. Perez-Omil, S.E. Collins, H. Okuno, J.J. Calvino, Critical influence of nanofaceting on the preparation and performance of supported gold catalysts, ACS Catal 5 (2015) 3504–3513, https://doi.org/10.1021/acscatal.5b00086.
[40] S. Fernández-García, S.E. Collins, M. Tinoco, A.B. Hungría, J.J. Calvino, M. A. Cauqui, X. Chen, Influence of {111} nanofaceting on the dynamics of CO adsorption and oxidation over Au supported on CeO2 nanocubes: An operando DRIFT insight, Catal. Today. 336 (2019) 90–98, https://doi.org/10.1016/j.cattod.2019.01.078.
[41] S. Fernandez-Garcia, L. Jiang, M. Tinoco, A.B. Hungria, J. Han, G. Blanco, J. J. Calvino, X. Chen, Enhanced hydroxyl radical scavenging activity by doping lanthanum in ceria nanocubes, J. Phys. Chem. C. 120 (2016) 1891–1901, https://doi.org/10.1021/acs.jpcc.5b09495.
[42] S.M. Collins, S. Fernandez-Garcia, J.J. Calvino, P.A. Midgley, Sub-nanometer surface chemistry and orbital hybridization in lanthanum-doped ceria nanocatalysts revealed by 3D electron microscopy, Sci. Rep. 7 (2017) 5406, https://doi.org/10.1038/s41598-017-05671-9.
[43] L. Jiang, S. Fernandez-Garcia, M. Tinoco, Z. Yan, Q. Xue, G. Blanco, J.J. Calvino, A. B. Hungria, X. Chen, Improved Oxidase Mimetic Activity by Praseodymium Incorporation into Ceria Nanocubes, ACS Appl. Mater. Interfaces. 9 (2017) 18595–18608, https://doi.org/10.1021/acsami.7b05036.
[44] X. Zhao, R. Long, Y. Chen, Z. Chen, Synthesis, characterization of CeO2@SiO2 nanoparticles and their oxide CMP behavior, Microelectron. Eng. 87 (2010) 1716–1720, https://doi.org/10.1016/j.mee.2009.09.012.
[45] I. Cabeza, L.G. Souto, J.M. Pintado, C. Pereira, C. Freire, G. Blanco, Influence of ceria distribution on the redox behaviour of nanoparticulated CeO2-SiO2 systems with application in catalysis, Surf. Interface Anal. 46 (2014) 712–715, https://doi.org/10.1002/sia.5499.
[46] A. Barroso-Bogeat, B. Núñez-Pérez, G. Blanco, J.M. Pintado, J.C. Hernández-Garrido, J.J. Calvino, Surface and redox characterization of new nanostructured ZrO2@CeO2 systems with potential catalytic applications, Surf. Interface Anal. 50 (2018) 1025–1029, https://doi.org/10.1002/sia.6444.
[47] S. Brunauer, P.H. Emmett, E. Teller, Adsorption of Gases in Multimolecular Layers, J. Am. Chem. Soc. 60 (1938) 309–319, https://doi.org/10.1021/ja01269a023.
[48] L.J. Allen, A.J. D'Alfonso, B. Freitag, D.O. Klenov, Chemical mapping at atomic resolution using energy-dispersive X-ray spectroscopy, MRS Bull 37 (2012) 47–52, https://doi.org/10.1557/mrs.2011.331.
[49] J.J. Sánchez, M. López-Haro, J.C. Hernández-Garrido, G. Blanco, M.A. Cauqui, J. M. Rodríguez-Izquierdo, J.A. Pérez-Omil, J.J. Calvino, M.P. Yeste, An atomically

efficient, highly stable and redox active Ce0.5Tb0.5Ox (3% mol.)/MgO catalyst for total oxidation of methane, J. Mater. Chem. A. 7 (2019) 8993–9003, https://doi.org/10.1039/c8ta11672e.
[50] H.P. Klug, L.E. Alexander, X-Ray Diffraction Procedures: For Polycrystalline and Amorphous Materials, 2nd ed., Wiley, New York, 1974.
[51] M. Thommes, K. Kaneko, A.V. Neimark, J.P. Olivier, F. Rodriguez-Reinoso, J. Rouquerol, K.S.W. Sing, Physisorption of gases, with special reference to the evaluation of surface area and pore size distribution (IUPAC Technical Report), Pure Appl. Chem. 87 (2015) 1051–1069, https://doi.org/10.1515/pac-2014-1117.
[52] M.A.L. Cordeiro, W. Weng, D.G. Stroppa, C.J. Kiely, E.R. Leite, High resolution electron microscopy study of nanocubes and polyhedral nanocrystals of cerium(IV) oxide, Chem. Mater. 25 (2013) 2028–2034, https://doi.org/10.1021/cm304029s.
[53] I. Florea, C. Feral-Martin, J. Majimel, D. Ihiawakrim, C. Hirlimann, O. Ersen, Three-dimensional tomographic analyses of CeO2 nanoparticles, Cryst. Growth Des. 13 (2013) 1110–1121, https://doi.org/10.1021/cg301445h.
[54] Y. Lin, Z. Wu, J. Wen, K.R. Poeppelmeier, L.D. Marks, Imaging the atomic surface structures of CeO2 nanoparticles, Nano Lett 14 (2014) 191–196, https://doi.org/10.1021/nl403713b.
[55] M. Tinoco, S. Fernandez-Garcia, A. Villa, J.M. Gonzalez, G. Blanco, A.B. Hungria, L. Jiang, L. Prati, J.J. Calvino, X. Chen, Selective oxidation of glycerol on morphology controlled ceria nanomaterials, Catal. Sci. Technol. 9 (2019) 2328–2334, https://doi.org/10.1039/c9cy00273a.
[56] P.A. Crozier, R. Wang, R. Sharma, In situ environmental TEM studies of dynamic changes in cerium-based oxides nanoparticles during redox processes, Ultramicroscopy 108 (2008) 1432–1440, https://doi.org/10.1016/j.ultramic.2008.05.015.
[57] M. Nolan, S.C. Parker, G.W. Watson, The electronic structure of oxygen vacancy defects at the low index surfaces of ceria, Surf. Sci. 595 (2005) 223–232, https://doi.org/10.1016/j.susc.2005.08.015.
[58] T. Tabakova, L. Ilieva, I. Ivanov, M. Manzoli, R. Zanella, P. Petrova, Z. Kaszkur, Structure-activity relationship in water-gas shift reaction over gold catalysts supported on Y-doped ceria, J. Rare Earths. 37 (2019) 383–392, https://doi.org/10.1016/j.jre.2018.07.008.
[59] H.C. Yao, Y.F.Y. Yao, Ceria in Automotive Exhaust Catalysts. I. Oxygen Storage, J. Catal. 86 (1984) 254–265, https://doi.org/10.1016/0021-9517(84)90371-3.
[60] T. Désaunay, G. Bonura, V. Chiodo, S. Freni, J.-P. Couzinié, J. Bourgon, A. Ringuedé, F. Labat, C. Adamo, M. Cassir, Surface-dependent oxidation of H2 on CeO2 surfaces, J. Catal. 297 (2013) 193–201, https://doi.org/10.1016/j.jcat.2012.10.011.
[61] V. Perrichon, A. Laachir, G. Bergeret, R. Fréty, L. Tournayan, O. Touret, Reduction of cerias with different textures by hydrogen and their reoxidation by oxygen, J. Chem. Soc. Faraday Trans. 90 (1994) 773–781, https://doi.org/10.1039/FT9949000773.
[62] A. Auroux, A. Gervasini, Microcalorimetric study of the acidity and basicity of metal oxide surfaces, J. Phys. Chem. 94 (1990) 6371–6379, https://doi.org/10.1021/j100379a041.
[63] M.G. Cutrufello, I. Ferino, R. Monaci, E. Rombi, V. Solinas, Acid-base properties of zirconium, cerium and lanthanum oxides by calorimetric and catalytic investigation, Top. Catal. 19 (2002) 225–240, https://doi.org/10.1023/A:1015376409863.
[64] S. Bernal, G. Blanco, J.M. Gatica, J.A. Pérez-Omil, J.M. Pintado, H. Vidal, Chemical reactivity of binary rare earth oxides, in: G. Adachi, N. Imanaka, Z.C. Kang (Eds.), Bin. Rare Earth Oxides, Kluwer Academic Publishers, Dordrecht, 2005, pp. 9–56.
[65] C. Binet, M. Daturi, J.-C. Lavalley, IR study of polycrystalline ceria properties in oxidised and reduced states, Catal. Today. 50 (1999) 207–225, https://doi.org/10.1016/S0920-5861(98)00504-5.
[66] G.N. Vayssilov, M. Mihaylov, P. St. Petkov, K.I. Hadjiivanov, K.M. Neyman, Reassignment of the vibrational spectra of carbonates, formates, and related surface species on ceria: A combined density functional and infrared spectroscopy investigation, J. Phys. Chem. C. 115 (2011) 23435–23454, https://doi.org/10.1021/jp208050a.
[67] G. Finos, S. Collins, G. Blanco, E. Del Rio, J.M. Cíes, S. Bernal, A. Bonivardi, Infrared spectroscopic study of carbon dioxide adsorption on the surface of cerium-gallium mixed oxides, Catal. Today. 180 (2012) 9–18, https://doi.org/10.1016/j.cattod.2011.04.054.
[68] Z. Wu, A.K.P. Mann, M. Li, S.H. Overbury, Spectroscopic investigation of surface-dependent acid-base property of ceria nanoshapes, J. Phys. Chem. C. 119 (2015) 7340–7350, https://doi.org/10.1021/acs.jpcc.5b00859.
[69] E.-M. Köck, M. Kogler, T. Bielz, B. Klötzer, S. Penner, In situ FT-IR spectroscopic study of CO2 and CO adsorption on Y2O3, ZrO2, and yttria-stabilized ZrO2, J. Phys. Chem. C. 117 (2013) 17666–17673, https://doi.org/10.1021/jp405625x.
[70] S. Wang, L. Zhao, W. Wang, Y. Zhao, G. Zhang, X. Ma, J. Gong, Morphology control of ceria nanocrystals for catalytic conversion of CO2 with methanol, Nanoscale 5 (2013) 5582–5588, https://doi.org/10.1039/c3nr00831b.
[71] S. Bernal, G. Blanco, A. El Amarti, G. Cifredo, L. Fitian, A. Galtayries, J. Martín, J. M. Pintado, Surface basicity of ceria-supported lanthana. Influence of the calcination temperature, Surf. Interface Anal. 38 (2006) 229–233, https://doi.org/10.1002/sia.2224.
[72] H. Metiu, S. Chrétien, Z. Hu, B. Li, X. Sun, Chemistry of Lewis acid-base pairs on oxide surfaces, J. Phys. Chem. C. 116 (2012) 10439–10450, https://doi.org/10.1021/jp301341t.
[73] T. Staudt, Y. Lykhach, N. Tsud, T. Skála, K.C. Prince, V. Matolín, J. Libuda, Electronic structure of magnesia-ceria model catalysts, CO2 adsorption, and CO2 activation: A synchrotron radiation photoelectron spectroscopy study, J. Phys. Chem. C. 115 (2011) 8716–8724, https://doi.org/10.1021/jp200382y.
[74] P.M. Albrecht, D. Jiang, D.R. Mullins, CO2 adsorption as a flat-lying, tridentate carbonate on CeO2(100), J. Phys. Chem. C. 118 (2014) 9042–9050, https://doi.org/10.1021/jp501201b.
[75] A.R. Symington, R.M. Harker, M.T. Storr, M. Molinari, S.C. Parker, Thermodynamic Evolution of Cerium Oxide Nanoparticle Morphology Using Carbon Dioxide, J. Phys. Chem. C. 124 (2020) 23210–23220, https://doi.org/10.1021/acs.jpcc.0c07437.